Self-diffusion in plastic flow of amorphous solids

Kamran Karimi*

Department of Physics and Astronomy, University of Calgary, 2500 University Drive NW, Calgary, Alberta, Canada T2N 1N4

(Received 15 September 2019; published 30 December 2019)

We report on a particle-based numerical study of sheared amorphous solids in the dense slow flow regime. In this framework, deformation and flow are accompanied by critical fluctuation patterns associated with the macroscopic plastic response. The former is commonly attributed to the collective slip patterns that relax internal stresses within the bulk material and give rise to an effective *mechanical* noise governing the latter particle-level process. In this paper, the *avalanche*-type dynamics between plastic events is shown to have a strong relevance on the self-diffusion of tracer particles in the Fickian regime. As a consequence, strong size effects emerge in the effective diffusion coefficient that is rationalized in terms of avalanche size distributions and the relevant temporal occurrence.

DOI: 10.1103/PhysRevE.100.063003

I. INTRODUCTION

Plasticity in amorphous solids refers to intense (irrecoverable) shear deformation that the flowing material goes through macroscopically without any crushing or crumbling. The plastic flow and deformation are accompanied by intermittent spatiotemporal fluctuation patterns that have been recently described within the context of *yielding transition* [1]. The microscopic basis of the fluctuations relates to the appearance of Eshelby-like events, small-scale rearranging particles that relax internal stress locally but incur long-range elastic-type perturbations in the medium [2]. In the absence of thermal fluctuations, local isolated events are initially activated in driven systems, but then further instability may be triggered and propagates due to long-range interactions. The *non*local triggering mechanism leads to an *avalanche*like dynamics that reveal critical scale-free statistics. This includes power-law distributions of avalanche size and duration associated with diverging relevant length and/or timescales [3,4]. In this context, the failure phenomenon may be viewed as a true nonequilibrium transition with universal scaling properties [5].

Another important microscopic picture pertains to the diffuse nature of particle trajectories within sheared disordered solids, akin to a thermally assisted process. Based upon mean-field arguments, the observed diffusivity can be ascribed to the emergence of "mechanical noise" generated by large relaxation events. *A priori*, dynamics of plastic avalanches must have a strong bearing on the diffusion process down at microscales. Within this context, Martens *et al.* used a mesoscopic elastoplastic model to relate flow-induced heterogeneities and diffusion constant with regard to shearing rate sensitivity and finite size effects [6]. Using a related numerical model in Refs. [1,7], avalanche statistics were shown to be straightly linked to rheological flow properties based upon generic scaling arguments and a formal analogy with the depinning transition. Particle-based simulations revealed system-spanning slip patterns that were argued to govern long-time diffusive behavior [8–13]. Recent studies [14,15] report on the emergence of *anomalous* diffusion (Lévy flight, in particular) in driven amorphous solids that may be qualitatively understood in view of the broadly distributed mechanical noise released by scale-free relaxation events [16]. The observed superdiffusive dynamics was rationalized within the context of continuous time random walk theory [17] taking into consideration a Poissonian temporal process with broad "jump" size distributions.

Here, in this paper, our aim is to build a generic relationship between diffusivity and avalanche dynamics that should not be specific to microscopic constituents and/or interactions. In this framework, displacement fluctuations are shown to exhibit nontrivial scale-dependent features that could be quantified in terms of the magnitude and geometry corresponding with individual avalanches. We provide a mean-field-type prediction for the scaling observations based on the fact that the geometry of each slip event may be idealized as a collection of elementary Eshelby transformations. The interoccurrence time distributions, on the other hand, can be interpreted in terms of a Poisson point process with the activity rate that shows nontrivial scaling features. These mechanisms lead up to a long-time diffusionlike process that is characterized by a size-dependent diffusion constant.

The mean-field treatment we propose is based on the fact that stress avalanches in slowly driven systems exhibit strong fluctuations over a broad range of scales. This varying size may be associated with a few individual particles that abruptly rearrange or system-spanning slip lines. The latter scale can be taken as a "cutoff" length controlled by the distance to the (yielding) transition point and was referred to as a typical cooperative length [6] or a characteristic quasilinear avalanche scale [9,10]. In this framework, no or very small fluctuations were attributed to this effective size and a single avalanche size was used as a simplification in this mean-field picture. Our proposed approach, however, takes these missing ingredients into consideration with a direct reference to the true dynamics of plastic avalanches.

*kamran.karimi1@ucalgary.ca

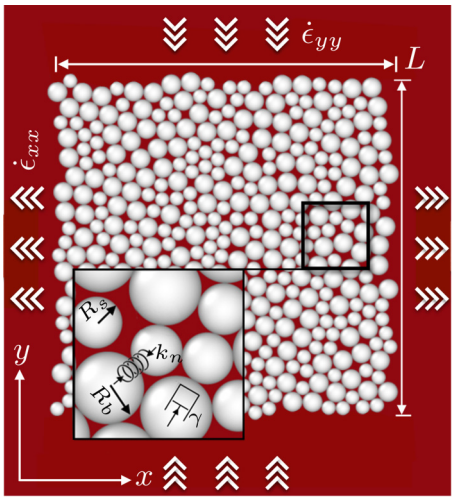

FIG. 1. Biaxial loading setup. The white disks (with radii R_s and R_b) represent the bulk sample with size L. The overlapping particles interact via a linear spring k_n as sketched in the inset. The dashpot represents the viscous dissipation contribution with drag ratio γ. The white arrows indicate the strain-controlled condition with a constant strain rate of $\dot{\epsilon}_{xx} = -\dot{\epsilon}_{yy} = \dot{\epsilon}$.

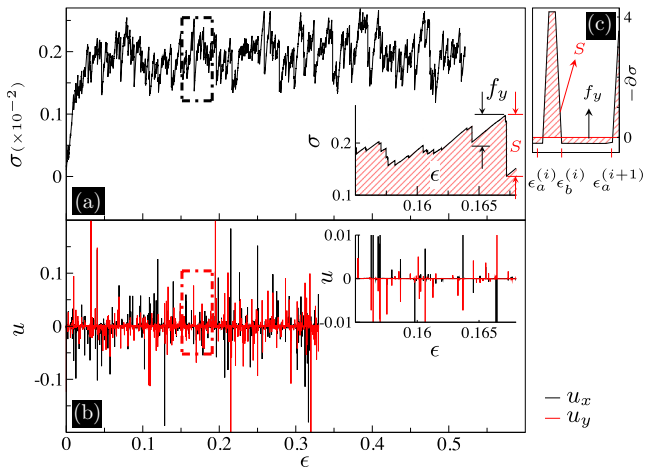

FIG. 2. Results of strain-controlled biaxial tests at $L = 80$. Evolution of (a) the bulk shear stress σ and (b) the tracer particle displacement u per unit time step along x and y with the imposed strain ϵ. The insets are the closeup views of the main graphs. (c) $-\partial_\epsilon\sigma$ versus ϵ corresponding to the ith avalanche. The hatched areas over $[\epsilon_a^{(i)}, \epsilon_b^{(i)}]$ and $[\epsilon_b^{(i)}, \epsilon_a^{(i+1)}]$ denote the avalanche size S and stress threshold f_y indicated by the corresponding arrows. The flat (red) line indicates $\partial_\epsilon\sigma = 0$.

The organization of the paper is as follows. In Sec. II, the biaxial shear setup, packing preparation, driving protocol, and relevant simulation details are discussed. In Sec. III, we quantify avalanche size fluctuations along with variations in tracer particles displacements. We use a mean-field level argument to link the two sets of statistics and validate the proposed scaling by numerical data. The interevent time distributions and associated scaling features will be the subject of Sec. IV. In Sec. V, the results from Secs. III and IV are integrated to describe the diffusion process that governs the long-term temporal dynamics.

II. MODEL AND PROTOCOL

We used bi-disperse packings of N two dimensional ($d = 2$) disks with radii R_s and R_b in a biaxial loading geometry illustrated in Fig. 1. We set $R_b/R_s = 1.4$ and $N_b/N_s = 1$ where $N_{b(s)}$ denotes the number of particles in each species. The ith and jth particles with position vectors $\vec{r}_i, \vec{r}_j$ may interact with each other when the overlap $\delta = R_i + R_j - |\vec{r}_i - \vec{r}_j| > 0$. The normal contact forces is $\vec{f}_n = -k_n\,\delta\vec{e}_n$ with the unit normal vector $\vec{e}_n = (\vec{r}_i - \vec{r}_j)/|\vec{r}_i - \vec{r}_j|$. Here, k_n is the normal spring constant. A linear drag force $\vec{f}_{\rm vis} = -m\tau_d^{-1}\vec{r}$ is applied on each particle with dissipation rate τ_d^{-1}. The rate unit (inverse timescale) is set by the vibrational frequency $\omega_n^2 = k_n/m$ where m denotes the particle mass. Newton's equations of motion were solved in LAMMPS [18],

$$m_i\ddot{\vec{u}}_i = \vec{f}_n + \vec{f}_{\rm vis}. \tag{1}$$

We also set the discretization time $\Delta t = 0.05\omega_n^{-1}$. An overdamped dynamics was imposed by setting a high value of the damping rate τ_d^{-1} (in comparison with the vibrational frequency ω_n).

Prior to shearing, samples were prepared by assigning N particles randomly in a biperiodic $L \times L$ square box with area fraction $\phi = L^{-2}\sum_{i=1}^{N}\pi R_i^2$. We set $\phi = 0.9$, well above the jamming threshold in two dimensional packings. A strain-controlled condition was then applied by deforming the periodic box along x and y at a constant strain rate $\dot{\epsilon}_{xx} = -\dot{\epsilon}_{yy} = \dot{\epsilon}$. The loading protocol was implemented in a discontinuous fashion to ensure the quasistatic condition. That is, the sample accommodates the incremental strain of $\dot{\epsilon}\,\Delta t$ each time step which is followed by a relaxation period with no further deformation (fixed L). The latter phase terminates once the total kinetic energy $K = \frac{1}{2}\sum_{i=1}^{N} m_i\vec{\dot{r}}_i\cdot\vec{\dot{r}}_i < 10^{-10}$ before the next loading period resumes. We checked that $\dot{\epsilon}$ was small enough that the stress condition was almost insensitive to the loading rate.

The results of the shear tests may be used to determine the bulk shearing strength together with the structure of deformation during plastic flow. The macroscopic stress tensor is defined as

$$\sigma_{\alpha\beta} = L^{-d}\sum_i\sum_{i<j}(\vec{f}_{ij}\otimes\vec{r}_{ij})_{\alpha\beta}, \tag{2}$$

using the Kirkwood-Irvine expression [19] where $\vec{f}_{ij} = \vec{f}_n$ and $\vec{r}_{ij} = \vec{r}_i - \vec{r}_j$. We also compute the nonaffine displacement $\vec{u}_i = \vec{u}_i^{\rm tot} - \vec{u}_i^{\rm aff}$ of the ith tracer particle accumulated over time step Δt with the total displacement $\vec{u}_i^{\rm tot} = \vec{r}_i(t+\Delta t) - \vec{r}_i(t)$ and affine contribution $\vec{u}_i^{\rm aff} = \dot{\epsilon}\,\Delta t(\vec{e}_x\otimes\vec{e}_x - \vec{e}_y\otimes\vec{e}_y)\{\vec{r}_i(t) - \vec{r}_o\}$. Here, $\vec{r}_o$ and $\vec{e}_{x(y)}$ denote the position vector of the box center and unit vector along $x(y)$, respectively.

The resulting load curves $\sigma = \frac{1}{2}(\sigma_{xx} - \sigma_{yy})$ against shear strain $\epsilon = \frac{1}{2}(\epsilon_{xx} - \epsilon_{yy})$ are reported in Fig. 2(a). Figure 2(b) shows the nonaffine displacements u of a tracer particle along x and y which are accumulated over one time step (or the duration of one single avalanche). Upon shear loading, the response reveals a well-established steady flow in Fig. 2(a) following the initial yielding regime. As evidenced in the

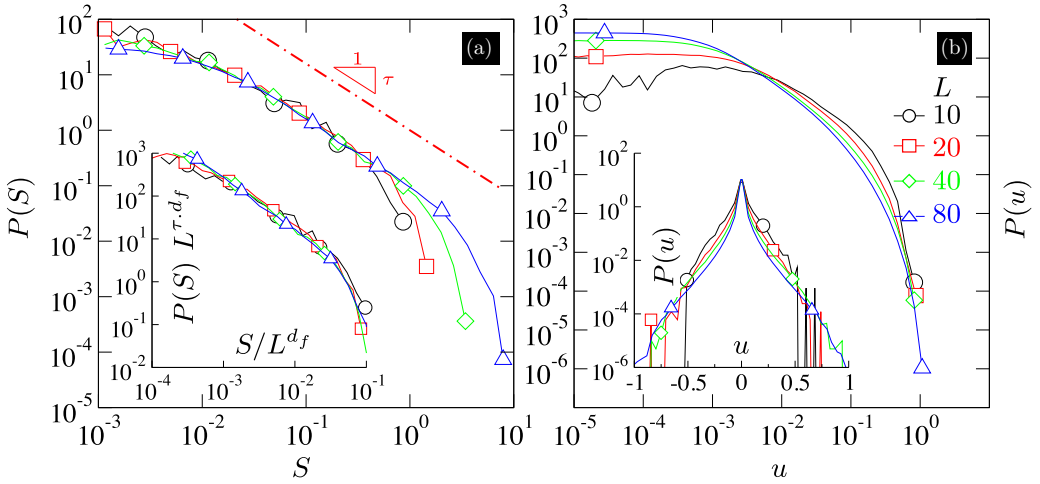

FIG. 3. Statistics of (a) avalanche sizes S and (b) particle displacements u at multiple system sizes $L = 10, 20, 40, 80$. The dashed-dotted line indicates a power-law $S^{-\tau}$ with $\tau = 1.20 \pm 0.09$. The left inset plots the rescaled distributions $P(S)L^{\tau d_f}$ versus S/L^{d_f} with $d_f = 1.05 \pm 0.05$. The right inset is the same as the main graph in (b) but plotted on the log-linear scale.

upper inset of Fig. 2(a), the stress dynamics is characterized by abrupt falloffs which are preceded by longer periods of stress buildup, an expected feature of amorphous structures. This bursty dynamics becomes further apparent in $\partial_\epsilon \sigma$, the derivative of the stress signal with respect to strain, which is shown in the lower inset of Fig. 2(a). Figure 2(b) shows intermittent features that are also present in the tracer particle trajectory and appear to statistically correlate with the extent of stress drops as the deformation proceeds. The latter, indeed, relates to the avalanche size $S \doteq -L^d \int_{\epsilon_a^{(i)}}^{\epsilon_b^{(i)}} \partial_\epsilon \sigma \, d\epsilon$ which has dimensions of energy and corresponds to the ith avalanche incurred at the strain interval $[\epsilon_a^{(i)}, \epsilon_b^{(i)}]$ as sketched in Fig. 2(c). Another fluctuating quantity is the stress threshold $f_y \doteq \int_{\epsilon_b^{(i)}}^{\epsilon_a^{(i+1)}} \partial_\epsilon \sigma \, d\epsilon$ which measures the amount of stress the system can accumulate between the ith and the $(i+1)$st avalanche over the strain period $[\epsilon_b^{(i)}, \epsilon_a^{(i+1)}]$. The stress threshold f_y together with the tracer displacement u and avalanche size S show nontrivial statistics which will be the subject of the following sections.

III. PARTICLE DISPLACEMENT STATISTICS

The statistical metric we probe is the probability distribution function for plastic avalanches $P(S)$ and particle displacements $P(u)$. Due to the loading symmetry along x and y, the corresponding displacements are *statistically* equivalent and we, accordingly, drop the subscript for u hereafter. The statistics are collected independently over multiple sheared samples once a steady-state flow regime was established following an initial transient response, i.e., $\epsilon > 0.1$. We used the full set of particles and associated trajectories so as to improve particle-based statistics.

In Fig. 3(a), we show avalanche size statistics $P(S)$ scaling as a power-law $P(S) \propto S^{-\tau}$ with over almost three decades. The steep decay at large S values is a signature of extended system-spanning events that will typically scale with the physical size of the sample, i.e., L^{d_f}. In the inset of Fig. 3(a), the distribution of avalanche sizes is collapsed using $\tau = 1.20 \pm 0.09$ and $d_f = 1.05 \pm 0.05$ (cf. Appendix A). The former exponent is reasonably close to the mean-field prediction of $\tau = \frac{3}{2}$ [7]. The latter denotes the fractal dimension quantifying the spatial extension of slip events. The preliminary plateau regime corresponds to localized shear modes that would naturally depend on microscopic details rather than linear size L.

As for particle displacement distributions in Fig. 3(b), $P(u)$ does not seem to include critical scaling features present in avalanche size statistics. The data develop a cusp in the center which extends to an exponential decay at intermediate and large u values as illustrated in the inset of Fig. 3(b). The typical scale (of order unity or particle size) within the exponential tail corresponds with the geometry of locally rearranging particles which is analogous to "T1" events in foam dynamics [20]. This upper bound is, therefore, almost insensitive to the macroscopic size L as reported in Ref. [8]. However, size effects are evident in terms of distribution widths with larger samples containing weaker displacement fluctuations.

We further examined the root mean squared fluctuations $\langle u^2|S\rangle^{1/2}$ conditioned on avalanche size S. Apart from the plateau region at small values of S, the scatter plot of Fig. 4(a) indicates that avalanches with larger magnitudes will, in general, result in a broader *noise* distribution. We noted similar trends in a model metallic glass where the crossover behavior was associated with the interplay between small and large events [21]. The data collapse in Fig. 4(b) signifies that the width of distributions is uniquely determined by the rescaled avalanche size S/L^{d_f}.

We rely on a mean-field approximation introduced in Ref. [10] to explain the observed scaling behavior associated with displacement fluctuations. Within this approach, avalanches are effectively treated as quasilinear objects in two dimensional space ($d = 2$) extended over size ξ within a system of linear size L. This fractal unit is assumed to be constructed by a set of individual Eshelby elements that incur decaying displacements of the form $u \propto 1/r^{d-1}$ in the elastic medium [22]. Superimposing individual contributions,

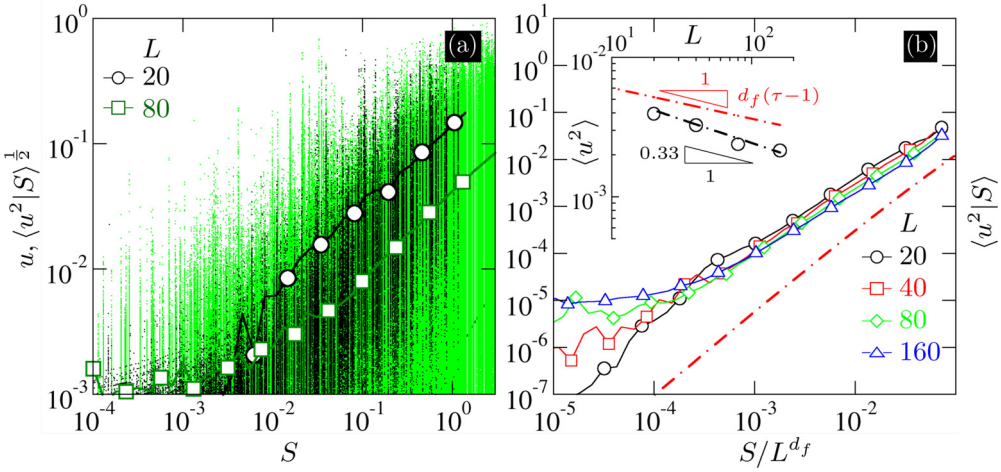

FIG. 4. Statistics of tracer particles motion conditioned on avalanche size S at different sample sizes L. (a) Scatter plot of the correlations between displacements u and S at $L = 20, 80$. The solid curves show conditional variance $\langle u^2|S\rangle$ plotted against S, (b) $\langle u^2|S\rangle$ versus S/L^{d_f} at $L = 10, 20, 40, 80$. The dashed-dotted line indicates the $\langle u^2|S\rangle \propto -(S/L^{d_f})^{2/d_f}\ln(S/L^{d_f})$ scaling with $d_f = 1.05$. The inset plots the expected variance $\langle u^2\rangle$ against L. The dashed-dotted (red) line is a guide to the power-law $\langle u^2\rangle \propto L^{-d_f(\tau-1)}$ with $\tau = 1.2$. The lower dashed-dotted (black) line indicates the measured slope based on the least-squares regression.

it follows that:

$$u(r|\xi) = \int_{x=-(\xi/2)}^{+(\xi/2)} \frac{1}{|r-x|^{2-1}}dx \propto \tanh^{-1}\left(\frac{\xi}{r}\right), \qquad r > \frac{\xi}{2}, \tag{3}$$

which shows a slow logarithmic decay in the near field. Note that the $u \propto 1/r$ scaling will be recovered using the far-field approximation at $r \gg \xi$.

The displacement distribution conditioned on size ξ will be given as

$$P(u|\xi) = \int_{r=\xi/2}^{L} \delta\left[u - \tanh^{-1}\left(\frac{\xi}{r}\right)\right]d^d r \propto \frac{\cosh(u)}{\sinh^3(u)}, \qquad \tanh^{-1}\left(\frac{\xi}{L}\right) < u < \infty, \tag{4}$$

with the lower cutoff set by the finite system size. Therefore,

$$\langle u^2|\xi\rangle = \int u^2 P(u|\xi)du \propto -\left(\frac{\xi}{L}\right)^2 \ln\left(\frac{\xi}{L}\right) + O\left[\left(\frac{\xi}{L}\right)^3\right], \quad \xi \ll L. \tag{5}$$

Inserting $\xi \propto S^{1/d_f}$, the proposed scaling is plotted in Fig. 4(b) which appears to slightly overestimate the power-law-like growth of fluctuations. Here, we note that the existence of (anti) correlations between individual avalanches might result in higher order contributions to Eq. (5) which is currently derived based on the hypothesis of *independence* between plastic events. Furthermore, the methodology assumes a simple fractal geometry of stress avalanches which is not necessarily descriptive of more complex objects with multifractal topology.

Contrary to Ref. [10], which considered a single avalanche size, we explicitly take into account the distribution of avalanche sizes and their individual contributions. Given the above functional forms, the expected variance $\langle u^2\rangle = \int\langle u^2|S\rangle P(S)dS$ should now scale as $\langle u^2\rangle \propto 1/L^{d_f(\tau-1)}$. The derived scaling relation indicates that a reduction in τ will amplify fluctuations which is meaningful since shallow avalanche distributions imply high occurrence frequencies of large avalanches. The numerical data agree pretty well with theoretical predictions as in the inset of Fig. 4(b) indicating the strong relevance of stress fluctuation patterns (and associated critical exponents) on single particle statistics. In this framework, our Eshelby-based methodology differs from previously reported approaches [6,9] which inferred the mean-squared displacements based on a *characteristic* avalanche hypothesis ignoring the full avalanche size distributions. This might be a valid assumption at finite driving rates and/or in the presence of thermal fluctuations which, in general, tend to suppress scale-free statistics [23].

IV. "WAIT TIME" DISTRIBUTIONS

Statistically speaking, the temporal characteristics of single particle diffusion should pertain to the dynamics of stress avalanches as is qualitatively seen in Fig. 2. Stress drops tend to be well coincided with intensely rearranging tracer particles. The *quiescent* intervals in u, on the other hand, correspond closely with the accumulation periods of bulk stress.

In the framework of the yielding transition, this interevent dynamics is commonly quantified via the instability threshold f_y. Figure 5 quantifies fluctuations in this quantity at multiple system sizes. In Figs. 5(b) and 5(c), the exponential decay of our data, i.e., $P(f_y) = \bar{f}_y^{-1}\exp(-f_y/\bar{f}_y)$, suggests a Poissonian nature of the underlying yielding mechanism. The data collapse of Fig. 5(a) validates this hypothesis. The inset of Fig. 5(a) confirms that the mean stress threshold $\bar{f}_y$ decays with system size L. The associated scaling exponent follows from the stress conservation argument, i.e., $\langle\dot{\sigma}\rangle = 0$ which

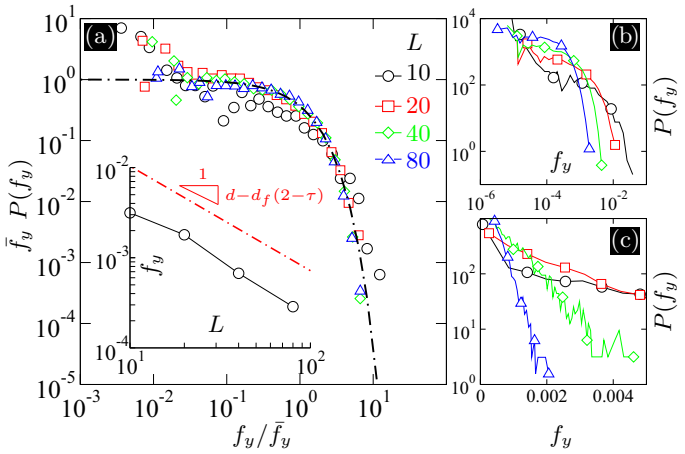

FIG. 5. Statistical behavior of the failure threshold f_y at different sizes $L = 10, 20, 40, 80$. (a) Rescaled distributions $\bar{f}_y P(f_y)$ plotted against $f_y/\bar{f}_y$. (b) Threshold distributions $P(f_y)$ on the log-log scale. (c) $P(f_y)$ versus f_y on the log-linear scale. The inset plots the mean threshold value $\bar{f}_y$ against L. The dashed-dotted (red) line is a guide to power-law $\bar{f}_y \propto 1/L^{d-d_f(2-\tau)}$ with $d = 2$, $d_f = 1.05$, and $\tau = 1.2$. The (black) dashed-dotted curve in the main plot indicates an exponential decay.

results in $\bar{f}_y = L^{-d}\langle S\rangle$. The mean avalanche size is given by [1]

$$\langle S\rangle = \int SP(S)dS \propto L^{d_f(2-\tau)}, \qquad 1 < \tau < 2, \tag{6}$$

and, therefore, $\bar{f}_y \propto 1/L^{d-d_f(2-\tau)}$. Lower τ exponents (or equivalently higher frequency of larger events) tend to increase $\bar{f}_y$, in accordance with the proposed scaling, as the system will have to accommodate further stress to compensate larger avalanche-induced energy losses.

V. DIFFUSIVE DYNAMICS

In previous sections, the emerging fluctuations as a consequence of intermittent stress relaxations were shown to include scaling characteristics that could be mainly interpreted in the plastic yielding framework. The long-term dynamics, however, may still enter a limiting Fickian regime which largely neglects short-lived correlation features leading to an effective Brownian process at infinite times.

In order to validate the diffusion-based picture, we analyzed the total nonaffine displacements $X = \sum_{i=1}^{N} u_i$ accumulated over N loading steps. Figure 6(a) displays the temporal evolution of X associated with several tracer particles. Such signals can be typically obtained by integrating over the fluctuating noise as in Fig. 2(b). The inset of Fig. 6(a) presents the power spectrum of the signal $\langle|\hat{X}(\omega)|^2\rangle$ decaying as ω^{-2}, an expected scaling for a Brownian-type noise. In the inset of Fig. 6(b), the probability distributions $P(X)$ are plotted at large strain values ϵ. The rescaled data in Fig. 6(b), $\epsilon^{1/2}P(X)$ versus $X/\epsilon^{1/2}$, collapse on a master curve indicating a Brownian diffusion process at long times.

Fluctuations in X will certainly depend on how frequent stress avalanches occur over the course of plastic flow. We further ignore tracers motion during elastic loading phase which are presumably small, compared to plastic deformations, making negligible contributions to the long-time particle diffusion. Accordingly, N may represent the total number of incurred events over a given strain interval ϵ and fluctuate in accordance with the Poisson distribution,

$$P(N;\epsilon) = \frac{(\lambda\epsilon)^N}{N!}\exp(-\lambda\epsilon), \tag{7}$$

with the event rate λ and mean number $\langle N\rangle = \lambda\epsilon$. Considering independent events, it follows that $\langle X^2|N\rangle = N\langle u^2\rangle$ and, therefore, $\langle X^2\rangle = \lambda\langle u^2\rangle\epsilon$. We additionally assume that $\bar{f}_y$ controls the yielding rate, i.e., $\lambda^{-1} \sim \bar{f}_y$. Inserting $\bar{f}_y \propto 1/L^{d-d_f(2-\tau)}$ and $\langle u^2\rangle \propto 1/L^{d_f(\tau-1)}$ gives $\langle X^2\rangle \propto L^{d-d_f}\epsilon$ with the *effective* diffusion constant scaling as $D \propto L^{d-d_f}$, in line with the derivation in Ref. [24].

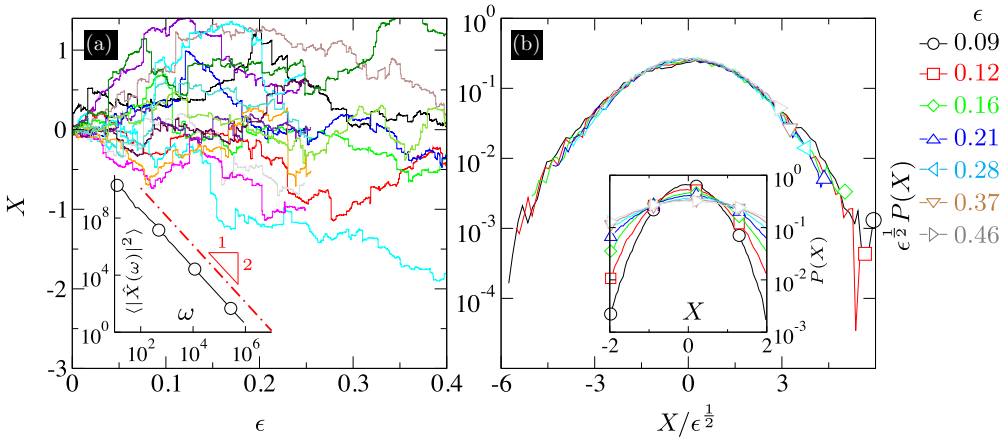

FIG. 6. Dynamics of the integrated noise $X = \sum_{i=1}^{N} u_i$ and relevant statistics at $L = 80$. (a) Accumulated displacements X incurred over the imposed strain ϵ corresponding to multiple tracer particles. The inset illustrates the associated power spectrum $\langle|\hat{X}(\omega)|^2\rangle$ in the frequency domain ω. The dashed-dotted line indicates $\langle|\hat{X}(\omega)|^2\rangle \propto \omega^{-2}$. (b) Rescaled probability distributions $\epsilon^{1/2}P(X)$ as a function of $X/\epsilon^{1/2}$ at different ϵ's. The inset shows the unrescaled data.

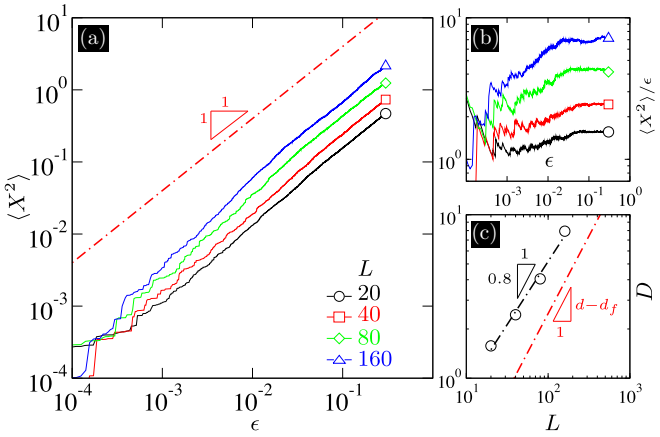

FIG. 7. Temporal evolution of the mean-squared displacement at multiple size L, (a) $\langle X^2 \rangle$ against ϵ. The dashed-dotted line with slope 1 indicates the linear growth $\langle X^2 \rangle \propto \epsilon$. (b) Rescaled quantity $\langle X^2 \rangle / \epsilon$ versus ϵ. (c) Size dependence of the effective diffusion coefficient D. The dashed-dotted line is a guide to power-law $D \propto L^{d-d_f}$ with $d = 2$ and $d_f = 1.05$.

Interestingly, D will have no dependence on τ, according to the derived relation, as this critical exponent makes equal contributions to the fluctuation size $\langle u^2 \rangle$ and average yielding time $\bar{f}_y$. This will result in a diffusion coefficient that is only sensitive to the topology of triggered avalanches (i.e., d_f at a fixed system size L). In other words, the size dependence will drop with uncorrelated avalanches filling up the entire space uniformly or equivalently $d \simeq d_f$.

Figure 7(a) examines the linear growth of the mean-squared displacements with ϵ within the steady-state flow regime. At all system sizes, $\langle X^2 \rangle$ exhibits a robust crossover to the Fickian regime at large strains, i.e., $\epsilon > 0.1$ (see Appendix B). The transition is more evident in Fig. 7(b) with $\langle X^2 \rangle / \epsilon$ reaching a size-dependent plateau as the deformation proceeds. The initial faster-than-diffusive regime can be attributed to the correlated elastic-type deformation that a marginally stable system accommodates up to a size-dependent threshold f_y. Figure 7(c) shows size effects associated with the effective diffusion coefficient along with the proposed finite-size scaling that seems to be robust over, at least, one order of magnitude. In Ref. [9], it was argued that, at the vanishing shear rate in two dimensions, the diffusion constant should scale as $D \propto L$ which is slightly different than the observed scaling. The discrepancy might come from different loading protocols, namely, the quasistatic loading and finite rate shearing in the limit of zero strain rate.

VI. CONCLUSIONS

We have analyzed the trajectories of individual particles in driven soft amorphous solids that exhibit scale-dependent fluctuation features both in terms of fluctuation amplitudes and in terms of occurrence frequencies. The observed properties were attributed to spatially extended avalanches that induce long-range deformation within the medium which can be quantified based on the concept of Eshelby shear transformations. The temporal dynamics, on the other hand, was described by introducing the stress instability threshold f_y, that is, on average, related to the mean avalanche size, as a result of the energy conservation principle. Fluctuations in f_y reveal a fast exponential-like decay which is at odds with broad scale-free avalanche-size distributions. The former exhibits a size-dependent characteristic stress scale $\bar{f}_y$ that must be linked with local energy "cages" in glassy structures [15]. The metastability hypothesis implies that fluctuations in local energy thresholds will be bounded as the driven solid always remain in *near*-critical states within the plastic flow regime [7]. Recent analysis of local yield stresses in sheared glasses made by Patinet *et al.* [25] led to narrow threshold distributions which is in agreement with this stability argument.

The scaling relations we have proposed are generic and potentially relevant for other disordered nonequilibrium systems that also show critical behavior but belong to a different universality class. For instance, Salerno *et al.* [26] argued that both inertial and overdamped samples have distinct but still critical avalanche size characteristics under steady shear. It would be interesting to validate our mean-field framework in the presence of inertia, particularly, in terms of jump size distributions and statistics of waiting times. It should be noted that the scaling of the diffusion factor could be quite different if the statistics of the avalanche size did not show scale-free regimes (i.e., due to thermal noise or finite shearing rate).

We have quantified displacement statistics by separating plastic avalanches and analyzing their individual contribution to diffusion. This will have important implications for a group of mean-field models that are formulated based on the notion of the mechanical noise, similar in essence to the Langevin dynamics with a stochastic source term that accounts for the effect of elastic couplings [27]. The structure of the input noise can be directly inferred from the statistics of stress avalanches (described by scaling exponents τ and d_f) which is commonly overlooked in current implementations. Another possible application could be in experimental contexts where accurate tracking of (small) individual particles is not feasible and, instead, the relevant statistical properties may be inferred from bulk stress measurements.

ACKNOWLEDGMENTS

We acknowledge insightful discussions with J.-L. Barrat, K. Martens, G. Gradenigo, and E. Bertin about our results.

APPENDIX A: AVALANCHE SIZE DISTRIBUTION

We have made a quantitative fitting analysis using the empirical relation $P(S) \propto \frac{1}{1+(\frac{S}{S_{\min}})^{\tau}} e^{-(S/S_c)^{\alpha}}$. The lower power-law cutoff $S_{\min}$ controls the roll-off at small avalanche sizes and is expected to scale as $S_{\min} \propto L^{-2}$. Here, $\alpha > 1$ describes the compressed exponential decay at $S > S_c$. Figure 8 plots the results of the maximum likelihood method and iterative curve fitting carried out at different system sizes L. We find $\alpha = 1.40 \pm 0.06$ and $\tau = 1.20 \pm 0.09$. The inset quantifies

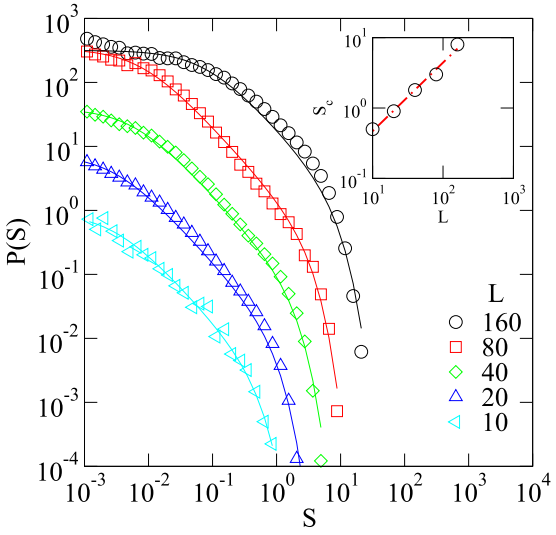

FIG. 8. Avalanche size distributions $P(S)$ at multiple system sizes $L = 160, 80, 40, 20, 10$. The solid curves indicate fits based on the functional form $P(S) \propto \frac{1}{1+(\frac{S}{S_{\min}})^{\tau}} e^{-(S/S_c)^{\alpha}}$. We find $\tau = 1.20 \pm 0.09$ using nonlinear curve fitting and the maximum likelihood method. The inset quantifies the scaling of the upper cutoff S_c with the system size L. The (red) dashed-dotted line indicates $S_c \propto L^{d_f}$ with $d_f = 1.05 \pm 0.05$.

the scaling of the upper cutoff S_c with the system size L. The (red) dashed-dotted line indicates $S_c \propto L^{d_f}$ with $d_f = 1.05 \pm 0.05$, in agreement with Refs. [7,26,28].

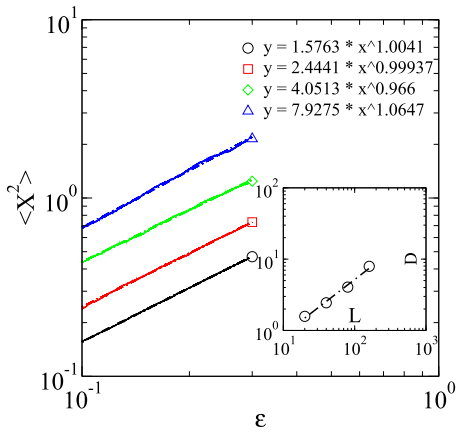

FIG. 9. Linear regression analysis of the mean-square displacement at multiple system sizes $L = 160, 80, 40, 20$ and large strains $\epsilon > 0.2$. The inset shows the prefactors D versus L. The dashed-dotted line indicates $D \propto L^{\alpha}$ with $\alpha = 0.80 \pm 0.07$.

APPENDIX B: MEAN-SQUARE DISPLACEMENTS

We have performed a regression analysis of the mean-square displacement at multiple system sizes L and large strains, i.e., $\epsilon > 0.1$. The power-law fits in Fig. 9 indicate $\langle X^2 \rangle = D\epsilon^{\beta}$ with the scaling exponent $\beta = 1.02 \pm 0.01$ and size-dependent prefactor D corresponding to the diffusive regime in the large strain limit.

[1] J. Lin, E. Lerner, A. Rosso, and M. Wyart, Scaling description of the yielding transition in soft amorphous solids at zero temperature, Proc. Natl. Acad. Sci. USA **111**, 14382 (2014).

[2] G. Picard, A. Ajdari, F. Lequeux, and L. Bocquet, Elastic consequences of a single plastic event: A step towards the microscopic modeling of the flow of yield stress fluids, Eur. Phys. J. E: Soft Matter Biol. Phys. **15**, 371 (2004).

[3] C. Liu, E. E. Ferrero, F. Puosi, J.-L. Barrat, and K. Martens, Driving Rate Dependence of Avalanche Statistics and Shapes at the Yielding Transition, Phys. Rev. Lett. **116**, 065501 (2016).

[4] P. Bak, C. Tang, and K. Wiesenfeld, Self-Organized Criticality: An Explanation of the $1/f$ Noise, Phys. Rev. Lett. **59**, 381 (1987).

[5] G. Parisi, I. Procaccia, C. Rainone, and M. Singh, Shear bands as manifestation of a criticality in yielding amorphous solids, Proc. Natl. Acad. Sci. USA **114**, 5577 (2017).

[6] K. Martens, L. Bocquet, and J.-L. Barrat, Connecting Diffusion and Dynamical Heterogeneities in Actively Deformed Amorphous Systems, Phys. Rev. Lett. **106**, 156001 (2011).

[7] J. Lin, A. Saade, E. Lerner, A. Rosso, and M. Wyart, On the density of shear transformations in amorphous solids, Europhys. Lett. **105**, 26003 (2014).

[8] C. E. Maloney and M. O. Robbins, Evolution of displacements and strains in sheared amorphous solids, J. Phys.: Condens. Matter **20**, 244128 (2008).

[9] A. Lemaître and C. Caroli, Rate-Dependent Avalanche Size in Athermally Sheared Amorphous Solids, Phys. Rev. Lett. **103**, 065501 (2009).

[10] A. Lemaître and C. Caroli, Plastic response of a two-dimensional amorphous solid to quasistatic shear: Transverse particle diffusion and phenomenology of dissipative events, Phys. Rev. E **76**, 036104 (2007).

[11] J. Chattoraj, C. Caroli, and A. Lemaitre, Robustness of avalanche dynamics in sheared amorphous solids as probed by transverse diffusion, Phys. Rev. E **84**, 011501 (2011).

[12] A. P. Roy, K. Karimi, and C. E. Maloney, Rheology, diffusion, and velocity correlations in the bubble model, arXiv:1508.00810.

[13] C. E. Maloney, Avalanches and diffusion in bubble rafts, Europhys. Lett. **111**, 28001 (2015).

[14] H. J. Hwang, R. A. Riggleman, and J. C. Crocker, Understanding soft glassy materials using an energy landscape approach, Nature Mater. **15**, 1031 (2016).

[15] F. Lechenault, R. Candelier, O. Dauchot, J.-P. Bouchaud, and G. Biroli, Super-diffusion around the rigidity transition: Lévy and the lilliputians, Soft Matter **6**, 3059 (2010).

[16] J. Lin and M. Wyart, Mean-Field Description of Plastic Flow in Amorphous Solids, Phys. Rev. X **6**, 011005 (2016).

[17] R. Metzler and J. Klafter, The random walk's guide to anomalous diffusion: A fractional dynamics approach, Phys. Rep. **339**, 1 (2000).

[18] S. Plimpton, Fast parallel algorithms for short-range molecular dynamics, J. Comput. Phys. **117**, 1 (1995).
[19] M. P. Allen and D. J. Tildesley, *Computer Simulation of Liquids* (Oxford University Press, Oxford, 2017).
[20] A. Kabla and G. Debrégeas, Local Stress Relaxation and Shear Banding in a Dry Foam Under Shear, Phys. Rev. Lett. **90**, 258303 (2003).
[21] P. Cao, K. A. Dahmen, A. Kushima, W. J. Wright, H. S. Park, M. P. Short, and S. Yip, Nanomechanics of slip avalanches in amorphous plasticity, J. Mech. Phys. Solids **114**, 158 (2018).
[22] K. Karimi and J.-L. Barrat, Correlation and shear bands in a plastically deformed granular medium, Sci. Rep. **8**, 4021 (2018).
[23] S. Karmakar, E. Lerner, I. Procaccia, and J. Zylberg, Statistical physics of elastoplastic steady states in amorphous solids: Finite temperatures and strain rates, Phys. Rev. E **82**, 031301 (2010).
[24] B. Tyukodi, D. Vandembroucq, and C. E. Maloney, Diffusion in Mesoscopic Lattice Models of Amorphous Plasticity, Phys. Rev. Lett. **121**, 145501 (2018).
[25] S. Patinet, D. Vandembroucq, and M. L. Falk, Connecting Local Yield Stresses with Plastic Activity in Amorphous Solids, Phys. Rev. Lett. **117**, 045501 (2016).
[26] K. M. Salerno, C. E. Maloney, and M. O. Robbins, Avalanches in Strained Amorphous Solids: Does Inertia Destroy Critical Behavior? Phys. Rev. Lett. **109**, 105703 (2012).
[27] E. Agoritsas, E. Bertin, K. Martens, and J.-L. Barrat, On the relevance of disorder in athermal amorphous materials under shear, Eur. Phys. J. E: Soft Matter Biol. Phys. **38**, 71 (2015).
[28] R. Arévalo and M. P. Ciamarra, Size and density avalanche scaling near jamming, Soft Matter **10**, 2728 (2014).